THE JOURNAL OF PHYSICAL CHEMISTRY C
A JOURNAL OF THE AMERICAN CHEMICAL SOCIETY

Open Access
This article is licensed under CC-BY 4.0

pubs.acs.org/JPCC
Article

Nano-Raman and Nano-Infrared Imaging of Dimerization of 4-Bromothiophenol on 2D Molybdenum Disulfide and Molybdenum Disulfide@Gold Hybrids

Published as part of The Journal of Physical Chemistry C special issue "Celebrating 50 Years of Surface Enhanced Spectroscopy."

Swati J. Patil and Dmitry Kurouski*

Cite This: https://doi.org/10.1021/acs.jpcc.4c05236
Read Online

ACCESS | Metrics & More | Article Recommendations | Supporting Information

ABSTRACT: Although metal dichalcogenides have unique optical and mechanical characteristics, they are 2D materials that as catalysts for light-driven reactions are yet to be fully understood. In this study, we used atomic force microscopy-infrared (AFM-IR) and tip-enhanced Raman (TER) spectroscopy to examine catalytic properties of 2D molybdenum disulfide (MoS2) synthesized by a hydrothermal approach as well as its hybrid with gold nanoparticles (MoS2@AuNPs). We found that both MoS2 and MoS2@AuNPs dehalogenase and dimerized 4-bromothiophenol (4-BTP) yielded thiophenol (TP) and 4,4′-biphenyldithiol (4,4′-BPDT), respectively. Although an equal yield of TP was observed on both MoS2 and MoS2@AuNPs, we observed a much greater yield of 4,4′-BPDT on MoS2@AuNPs compared with MoS2. These results demonstrated that metal dichalcogenides and their plasmonic hybrids could perform catalysis transformations previously evident for plasmonic metals such as gold and silver. Fabrication simplicity of metal dichalcogenides and their low costs open new avenues for synthetic approaches that can be used to develop a novel class of catalysts with the desired properties.

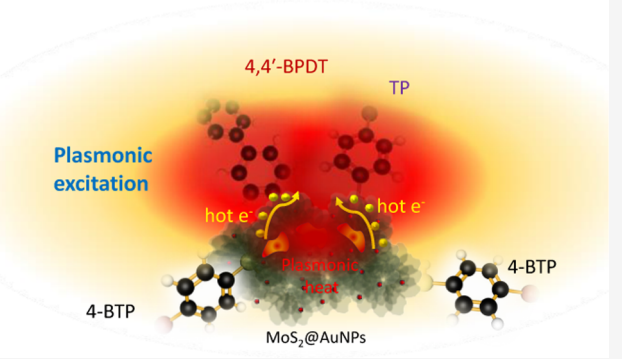

1. INTRODUCTION

Hot carriers are highly energetic species that can be injected into orbitals of molecules located in close proximity to metallic surfaces.[1−5] Hot carriers are produced as a result of a decay of localized surface plasmon resonances (LSPRs) and coherent oscillations of conductive electrons on the surfaces of nanostructures, which in turn are generated by light.[6−12] Most noble metal nanomaterials generate strong LSPRs.[13,14] However, their catalytic properties are limited to only a few reactions.[1−5] This limitation can be overcome by the use of catalytic metals in a reactor-antenna concept. Alternatively, both catalytic and plasmonic metals can coassembled in the core−shell or alloy bimetallic nanostructures.[15−18]

Two-dimensional (2D) nanomaterials, including metal dichalcogenides such as MX_2 (M = Mo, W, Nb, and X = S, Se, Te), attracted a broad interest for their excellent physical and chemical properties.[12,19] There has been a significant amount of interest in the development of these innovative materials for plasmonic catalysts and optoelectronics.[20−22] For instance, Li et al.[23] found that hydrothermally grown Au/graphene hydrogel could be used for the catalytic reduction of 4-nitrophenol (4-NP) to 4-aminophenol (4-AP).[24] Abid et al.[25] introduced a novel hybrid plasmonic metal-2D MXene-based Au@Ag@Pd/Ti_3C_2 photocatalyst for superior catalytic performance on plasmon-driven hydrogenation of nitro-aromatics. 2D materials have also shown intriguing potential for optoelectronics applications[26] such as light sources,[27] optical modulators,[28] photodetectors,[29] field-effect transistors,[30] logic circuits,[31] and sensors.[32−34]

A growing body of evidence indicates that optical and catalytic properties of 2D materials are determined by their nanostructure.[35−37] For instance, Rahaman et al.[38] demonstrated that 2D crystal/plasmonic heterostructure determined the local strain in MoS_2 during heterostructure formation. Using tip-enhanced Raman spectroscopy (TERS), Kalo et al.[39] showed that the nanoscale inhomogeneities such as defects and wrinkles in MoS_2 deteriorate the remarkable physical and optoelectronic properties of materials. In TERS, a metallized

Received: August 2, 2024
Revised: August 19, 2024
Accepted: September 9, 2024

Downloaded via 47.219.184.178 on September 27, 2024 at 23:30:00 (UTC).
See https://pubs.acs.org/sharingguidelines for options on how to legitimately share published articles.

© XXXX The Authors. Published by American Chemical Society

Scheme 1. (a). Schematic Illustration of the Synthesis of MoS_2 Nanomaterials and MoS_2@AuNPs Hybrids; (b) Nucleation and growth of MoS_2 Nanomaterials; (c) UV−Vis Absorbance Spectra of MoS_2, MoS_2@AuNPs, and AuNPs, and Enlarged View of MoS_2 and MoS_2@AuNPs as Shown in (d)

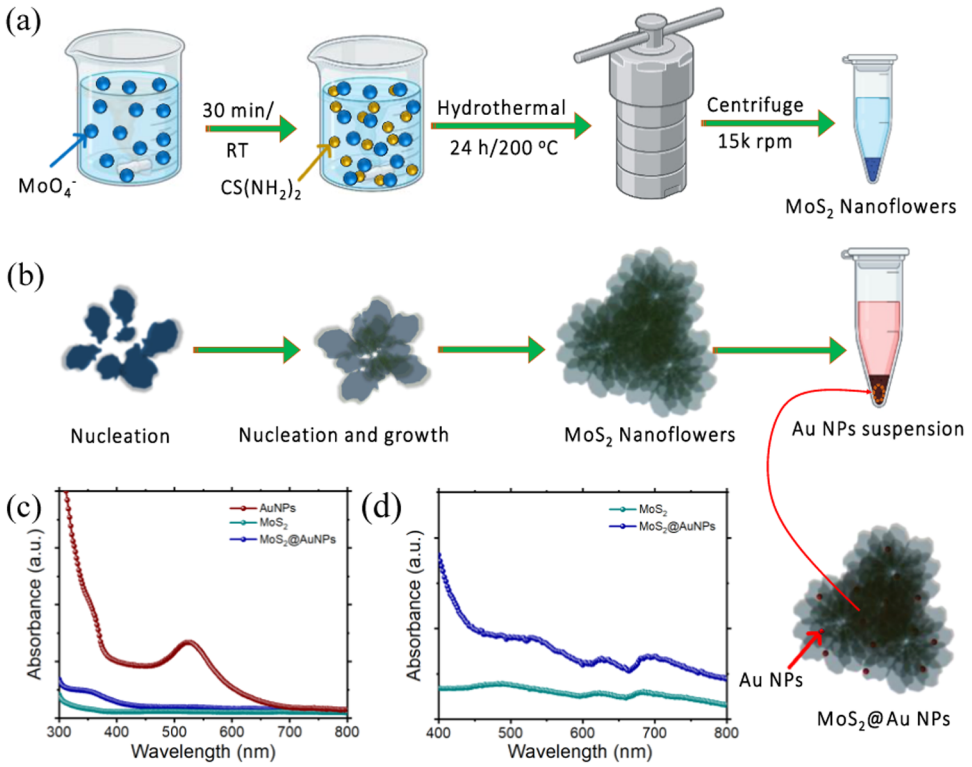

scanning probe is brought in close proximity to the sample of interest.[1−4] Next, the apex of the scanning probe is illuminated by light, which generates LSPRs at the metal surface.[5−12] LSPRs enhance Raman scattering from the molecules located directly under the tip up to a million-fold, which enables single-molecule sensitivity.[13,14] Furthermore, the electric field is confined under the tip down to a pico-volume. Therefore, if the tip is rastered above the sample, its chemical image can be recovered with subnanometer spatial resolution.

In this study, we used TERS to examine the nanoscale plasmonic and photocatalytic properties of MoS_2. For this, hydrothermally synthesized MoS_2 was modified with a monolayer of 4-bromothiophenol (4-BTP). Using TER, we found that 4-BTP on MoS_2 could be reduced to 4,4′-biphenyldithiol (4,4′-BPDT) and thiophenol (TP). We also found that the yield of this plasmon-driven reaction was enhanced when the surface of MoS_2 was decorated by AuNPs. We infer that the observed chemical transformations were driven by hot carriers, highly energetic species that could be directly or indirectly injected into molecular orbitals of molecular analytes. We also used atomic force microscopy-infrared (AFM-IR) spectroscopy, complementary to TER analytical technique, to confirm the observed TER chemical transformations on the surface of MoS_2, as well as its hybrid with gold nanoparticles (MoS_2@AuNPs). This technique allows for the identification of unknown characteristics through the use of absorption maps and point-specific spectra. Furthermore, it brings together the nanoscale spatial resolution offered by an AFM tip with the high chemical specificity of IR spectroscopy, and it has been studied on a wide range of samples.[40] In AFM-IR, a pulsed tunable IR laser causes thermal expansions in the sample that are recorded by the metallized scanning probe, which can be positioned on the object of interest.[41−44] Next, thermal expansions are converted into the IR spectrum.[9,45−47] Our group previously demonstrated the advantage of such a bimodal imaging approach in the analysis of complex biological systems.[48,49]

2. RESULTS AND DISCUSSION

We used a hydrothermal approach to synthesize MoS_2 nanomaterials from ammonium molybdate ($(NH_4)_6Mo_7O_{24}\cdot 4H_2O$) and thiourea ($NH_2CSNH_2$) (Scheme 1). In this reaction, Mo^{6+} in Mo_7O_{24} 6-ion was reduced to Mo^{4+}, which then reacted with H_2S to form MoS_2. The newly formed material is typically seen as an interlayer of S and Mo atoms covalently interconnected via weak van der Waals forces. Next, MoS_2 nanomaterials were decorated with AuNPs to synthesize MoS_2@AuNPs plasmonic hybrids. Using UV−vis spectroscopy, we found that MoS_2 had absorption bands at 486, 622, and 684 nm (Scheme 1(c,d)), whereas MoS_2@AuNPs exhibited an absorption band around 536 nm, which corresponds to LSPR of AuNPs.

The nanostructures of the synthesized MoS_2 and MoS_2@AuNPs were further characterized using field emission-scanning electron microscopy (FE-SEM) (Figure S1(a−d), respectively). FE-SEM images of both synthesized materials confirmed the uniform growth of nanoflower with a diameter of around 500 nm. The close-up view of the MoS_2 nanoflower-composed nanosheets consists of vertical-aligned nanolayers of MoS_2. In addition, the chemical composition and oxidation state of MoS_2@AuNPs were characterized by the X-ray photoelectron spectroscopy (XPS) technique, and results are provided in Figure S1(e−h). For the spectrum of MoS_2@AuNPs, it denotes four main peaks for Au 4f, S 2p, and Mo 3d

https://doi.org/10.1021/acs.jpcc.4c05236
J. Phys. Chem. C XXXX, XXX, XXX−XXX

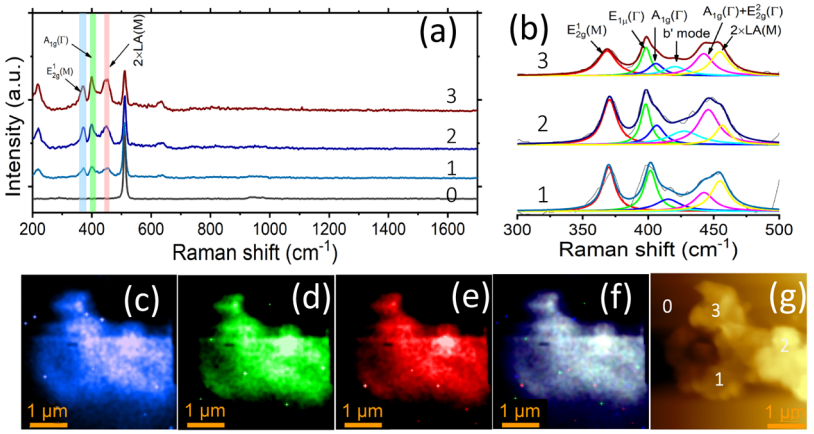

Figure 1. (a) Representative TERS spectra from dark and bright pixels in panel (f). (b) The TERS spectrum of MoS_2 highlighted point number shown in (g), deconvoluted using fitted Lorenz curves. TERS images of (c) E12g (M), (d) A1g (T), and (e) 2 × LA(M) in MoS_2. (f) TERS of mixed E12g (M), A1g (T), and 2 × LA(M) modes of MoS2. (g) The AFM image of MoS_2. The scale bar in each image is 1 μm.

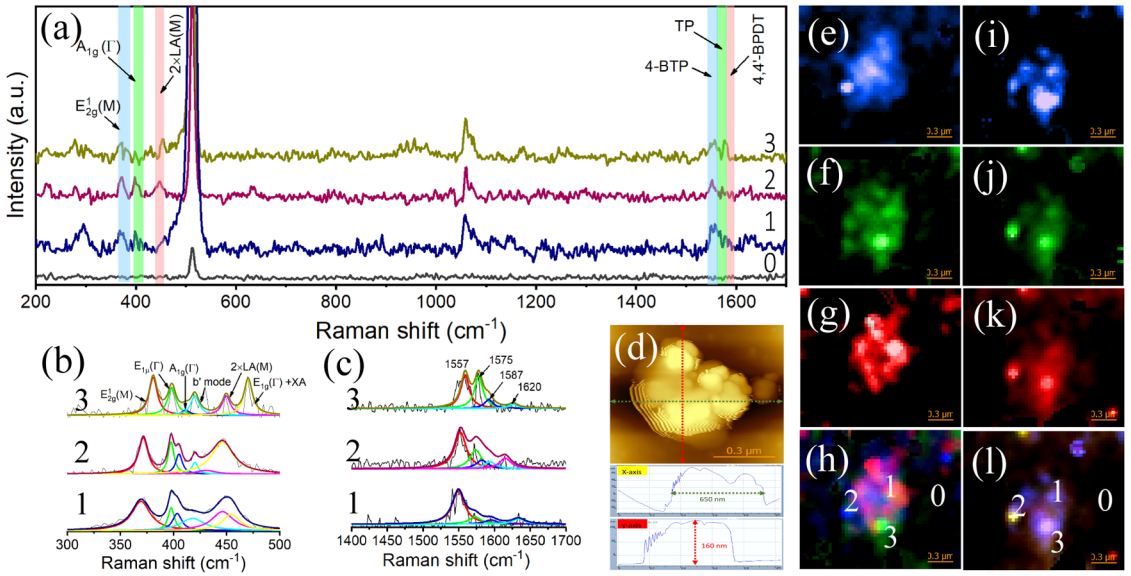

Figure 2. (a) Representative TER spectra of 4-BTP on the surface of MoS_2 collected at the outlined points from the map (l). (d) AFM topography of MoS_2. (b, c) TER spectra deconvoluted using Lorenz curves. (d) AFM and the corresponding TER image of 4-BTP-modified MoS_2: (e) $E_{2g}{}^1$, (f) A_{1g} (T), (g) 2 × LA(M), and (h) their overlay TER image of MoS_2. Optical and photocatalytic coupling of MoS_2: (i) 4-BTP (blue pixels) demonstrating the formation of (j) TP (green pixels) and (k) 4,4′-BPDT (red pixels). (l) An overlay TER image of 4-BTP, TP, and 4,4′-BPDT signals on MoS_2. The scale bar in each image is 300 nm.

(Figure S1(e)). As shown in Figure S1(f), the high-resolution Mo 3d spectra with doublet peaks at 228.1 and 231.72 eV are attributed to Mo $3d_{5/2}$ and Mo $3d_{3/2}$, respectively. S 2p XPS spectra (Figure S1(g)) that appear at 161.31 and 162.98 eV are associated with S $2p_{3/2}$ and S $2p_{1/2}$, respectively.[19] Au 4f spectrum as seen in Figure S1(h) exhibits peaks at 82.26 and 87.13 eV, which can be attributed to the doublet of Au 4f7/2 and Au 4f5/2, respectively. From these it is confirmed that AuNPs are in metallic state.[50,51]

We also used TERS to investigate the crystalline structures of MoS_2. TERS revealed the presence of four vibrational bands that corresponded to $E_1\mu$(M)-TA(M) at 204 cm^{-1}; E_{2g}(M) mode at 372 cm^{-1}; A_{1g} (T) mode at 401 cm^{-1}; and 2 × LA(M) at 459 cm^{-1} (Figure 1(a)). The strong in-plane E_{2g} mode originated from the out-of-plane vibrations of the S atoms with respect to the Mo atoms, whereas the A_{1g} (T) mode could be assigned to the out-of-plane vibration of the S atoms alone (Figure 1(b)).[52,53] The most intense mode around 459 cm^{-1} originated from the second-order process that involved the longitudinal acoustic phonons at the M point (LA(M)). The strong intensity of the LA(M) vibration in the acquired TER spectra indicated the multilayered nature of the synthesized MoS_2 nanosheets. TER maps of E12g (blue-pixel), A1g (T) (green-pixel), and 2 x LA(M) (red-pixel) are displayed in Figure 1(c–e), respectively, and the corresponding atomic force microscopy (AFM) image as shown in Figure 1(g).

Next, we used TERS to investigate the optical and photocatalytic properties of MoS_2. For this, MoS_2 nanomaterials were exposed to 4-BPT that formed a monolayer on their surfaces. TERS spectra acquired from such MoS_2 exhibited vibrational bands at 1064 and 1555 cm^{-1}, which could be assigned to the C−Br and C−C stretching modes of the benzene ring of 4-BTP, respectively.[54] In addition to the vibrational fingerprint of 4-BTP, we also observed vibrational bands at 1575 and 1585 cm^{-1}, which corresponded to TP and

https://doi.org/10.1021/acs.jpcc.4c05236
J. Phys. Chem. C XXXX, XXX, XXX−XXX

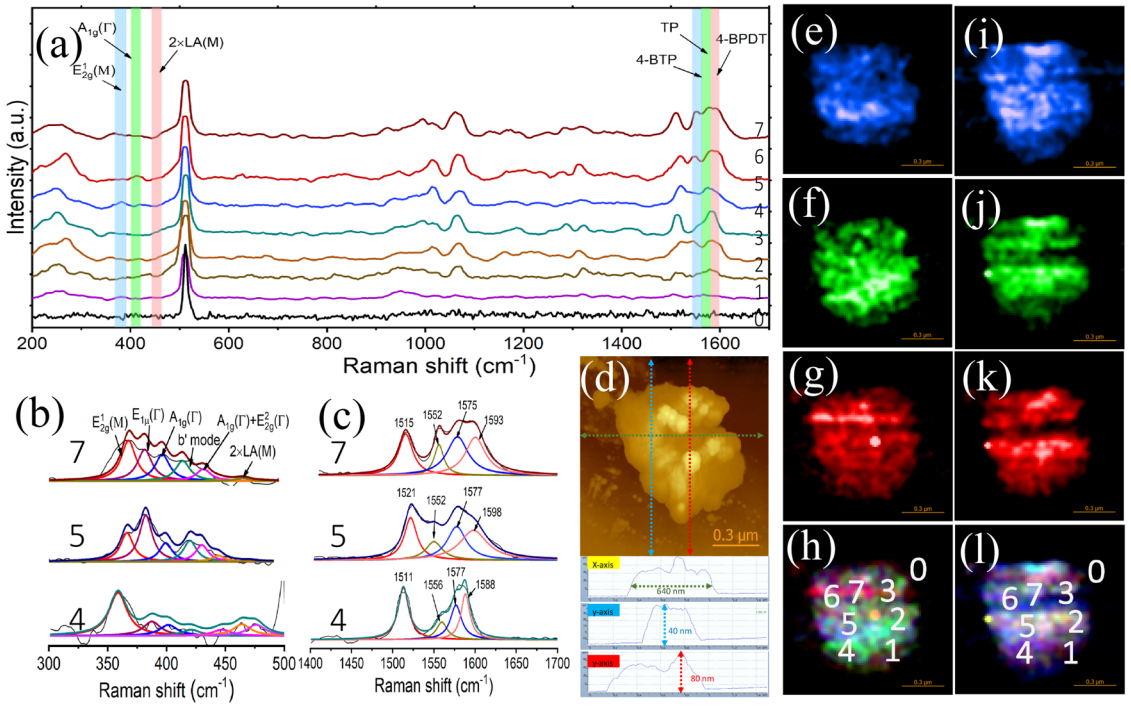

Figure 3. (a) Representative TER spectra of 4-BTP on the surface of MoS_2@AuNPs. (b, c) TER spectra deconvoluted using the Lorentzian approach at outlined points in maps (h, l). (d) AFM topography of MoS_2@AuNPs. TER mapping of 4-BTP-modified MoS_2 AuNPs: (e) $E_{2g}{}^1$ (M), (f) A_{1g} (T), (g) 2 × LA(M), and (h) their overlay. Optical and photocatalytic coupling of MoS_2@AuNPs: (i) 4-BTP (blue pixels) demonstrating the formation of (j) TP (green pixels) and (k) 4,4′-BPDT (red pixels). (l) An overlay of 4-BTP, TP, and 4,4′-BPDT signals. The scale bar in each image is 300 nm.

4,4′-BPDT, respectively (Figure 2 (a, b)).[18,55] These results demonstrated that MoS_2 enabled photocatalytic reduction of 4-BTP to both TP and 4,4′-BPDT. Finally, the acquired TER spectra also possessed the above-discussed $E_{2g}{}^1$(M), A_{1g} (T), and 2 × LA(M) modes of MoS_2 (Figure 2(b)). TERS imaging revealed a largely uniform distribution of the intensity of the vibrational bands originated from MoS_2 (Figure 2(e–h)). However, we did not observe the equal uniformity in the intensity of the vibrational bands that could be assigned to 4-BPT, TP, and 4,4′-BPDT (Figure 2(i–l)). Specifically, the edges and central parts of the MoS_2 nanosheets had a much higher intensity of 4-BTP than that of the thin nanolayer for MoS_2. These results showed that MoS_2 could be used to both dehalogenate and dimerize 4-BTP to form TP and 4,4′-BPDT, respectively. Our results also indicated that MoS_2 provided a strong gap-mode enhancement that was previously reported for plasmonic nano and microplates.[56,57]

Using TERS, we examined the optical properties of the MoS_2@AuNPs hybrids. TERS spectra acquired from MoS_2@AuNPs exhibited in-plane $E_{2g}{}^1$ (M) vibrational mode at ∼395 cm^{-1} together with the out-of-plane A_{1g} (T) mode at 404 cm^{-1} (Figure 3(a,b)). We also observed intense 2 × LA(M) mode at 465 cm^{-1} (Figure 3(a,b)). Thus, in the TERS spectra acquired from MoS_2@AuNPs, we observed a blue shift of these vibrational bands compared with their frequencies in the TERS spectra collected from MoS_2. Since $E_{2g}{}^1$ (M) represents the degree of structural distortion in MoS_2, one can expect that the observed blue shifts originated from the AuNPs-induced distortion of the van der Waals interactions between the layers of MoS_2.[58,59] TERS imaging of MoS_2@AuNPs revealed site-specific blue shifts of $E_{2g}{}^1$ (M), A_{1g} (T), and 2 × LA(M) modes (Figure 3(e–h)). However, we did not observe any correlation between the location of AuNPs and the blue shifts of the vibrational bands discussed above. Therefore, one can expect that the blue shift of $E_{2g}{}^1$ (M), A_{1g} (T), and 2 × LA(M) modes is caused by the exciton coupling between AuNPs and MoS_2. This expectation is further supported by the vanishing of AuNPs LSPR (∼520 nm) that is taking place upon their deposition on MoS_2 (Scheme 1(c)).

We used TERS to investigate the photocatalytic properties of MoS_2@AuNPs. Similar to the experiments discussed above with MoS_2, we exposed MoS_2@AuNPs to 4-BTP. TERS spectra acquired from 4-BTP-modified MoS_2@AuNPs exhibited vibrational bands at 1064 and 1555 cm^{-1}, as well as intense vibrational bands at 1575 and 1585 cm^{-1}, which corresponded to TP and 4,4′-BPDT, respectively (Figure 3(c)).[18,55] It should be noted that in the TERS spectra acquired from MoS_2@AuNPs, the intensities of 1064, 1555, 1575, and 1585 cm^{-1} bands were much greater compared with the intensities of these vibrational bands in the TERS spectra collected from MoS_2. These results indicate that MoS_2@AuNPs enabled much more efficient catalysis of 4-BTP compared with MoS_2. We also found that TERS imaging of MoS_2@AuNPs revealed largely uniform intensities of 1575 and 1585 cm^{-1} (Figure 3(i–l)), indicating that AuNPs-enhanced photocatalysis was not localized only on AuNPs, but rather was expanded to the entire volume of MoS_2@AuNPs. These findings are in good agreement with the previously reported results by Zhan et al.[60] Specifically, the researchers demonstrated that the presence of AuNPs in graphene rather than their abundance enabled the strong enhancement of the electric field in such nanomaterial.

We performed a quantitative analysis of the yield of 4,4′-BPDT on MoS_2 and MoS_2@AuNPs, as shown in Figure 4. For

https://doi.org/10.1021/acs.jpcc.4c05236
J. Phys. Chem. C XXXX, XXX, XXX−XXX

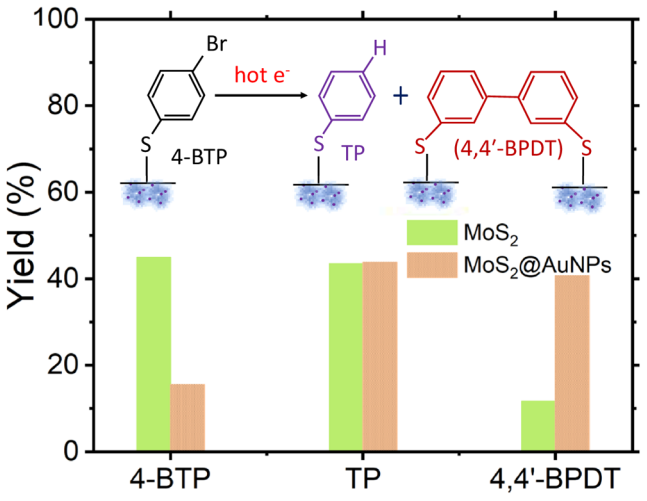

Figure 4. Bar diagram showing obtained yield of 4-BTP on MoS_2 and MoS_2@AuNPs surfaces; the inset shows the dehalogenase and dimerization of 4-BTP reaction pathway.

this, we counted the pixels in the above-discussed TER maps that possessed spectra with the vibrational signatures of 4,4′-BPDT, as well as the spectra that corresponded to TP. Previously reported results by our group showed that this approach could be used for a robust and reliable quantification of molecular species formed in plasmon-driven reactions.[11,66−69] We found that MoS_2@AuNPs demonstrated more than 3 times greater yield of 4,4′-BPDT compared with MoS_2. These results confirmed that MoS_2@AuNPs exhibited much greater catalytic reactivity compared with MoS_2. We also found that MoS_2@AuNPs and MoS_2 enabled equivalently efficient dehalogenation of 4-BTP that yielded TP. Experimental results recently reported by our and Chen's groups indicated that the 4-BTP dehalogenation yielded TP, which in turn reacted with another 4-BTP molecule to form 4,4′-BPDT.[18]

We also utilized AFM-IR, a complementary TERS approach, to investigate the photocatalytic properties of MoS_2 (Figure S5). AFM-IR point spectra obtained from the MoS_2 nanosheet exhibited five characteristic bands: 1407, 1466, 1543, 1691, and 1734 cm^{-1} (Figure S5(b−f)). Peaks at 1407 and 1618 cm^{-1} are attributed to MoS_2.[61] Peaks at 1466 and 1543 cm^{-1} originate from the stretching vibration of the C=C groups in the benzene ring of 4-BTP.[62] We also observed vibrational bands that could be assigned to phenol O−H bending (1310−1390 cm^{-1}), S=O stretching (1407 cm^{-1}),[63] aromatic C−H bending (1438 cm^{-1}), C=C stretching (1566−1650 cm^{-1}), and C=O stretching (1734 cm^{-1}).[64,65] These results demonstrate that AFM-IR could be used to probe the chemical structure of MoS_2, as well as detect 4-BTP on their surfaces.

As seen in Figure S6a, single-point AFM-IR spectra exhibited vibrational signatures of C−H bending, C=C stretching, and C=O stretching. The observed differences in the characteristic bands' intensity were attributed to the effects of 4-BTP demineralization on the surface of MoS_2 with Au surrounding. By a comparison of the AFM topography map of MoS_2@AuNPs with the height of the nanosheets, it can be seen that these disparities directly relate to the height of the nanosheets. At thicker regions of MoS_2@AuNPs, we observed a stronger intensity of AFM-IR spectra.

Recently reported results by the Raschke group demonstrate that the observed catalytic reactivity of both MoS_2 and MoS_2@AuNPs could be caused by excitons.[66−69] Specifically, the presence of dark excitons that have an antiparallel spin configuration with generally forbidden radiative emission. Park and co-workers demonstrated that coupling of a plasmonic scanning probe with WS_2 resulted in a high yield of dark excitons.[68,69] Our results indicate that dark excitons are highly likely to trigger chemical transformation in 4-BTP present on the surface of MoS_2 and MoS_2@AuNPs. Thus, excitons can perform chemical transformations in molecular analytes that were previously evident only for hot carriers.[10,11] It should be noted that exciton−plasmon coupling can be expected between MoS_2 and AuNPs that are present in MoS_2@AuNPs, which results in a much greater yield of 4,4′-BPDT that was observed on these hybrids compared with MoS_2 alone.[70−72] One can expect that in this case, excitons can trigger plasmon resonances on AuNPs that decaying will form hot carriers.[5−7] In turn, these highly energetic species cause dimerization of 4-BTP on MoS_2@AuNPs. However, in the previously reported study, we demonstrated that such dimerization was not possible on AuNPs, but rather required the presence of catalytic metals, such as Ni.[73] Based on these results, we can conclude that 4-BTP dimerization is catalyzed by MoS_2, while catalytic potential is enhanced on MoS_2@AuNPs by AuNPs-provided exciton−plasmon coupling.

3. EXPERIMENTAL SECTION/METHODS

3.1. Chemicals. All chemical reagents were purchased and used without further purification.

3.2. MoS_2 Synthesis. The chemical synthesis of MoS_2 nanomaterial was obtained by hydrothermal technique. To prepare MoS_2 nanomaterials, initially 10 mg of ammonium molybdate tetrahydrate ($(NH_4)_6Mo_7O_{24}{\cdot}4H_2O$) was added in 40 mL of distilled water and kept on a magnetic stirrer for 30 min to get a clear solution. Further, 4 mM thiourea (NH_2CSNH_2) was dissolved in the Mo-contained solution under constant magnetic stirring for a further 30 min. In the second step, the prepared final solution was transferred to a 50 mL capacity of Teflon-lined stainless-steel autoclave and kept at 200 °C for 24 h, and after completing reaction, it was allowed to cool down naturally. Further, the obtained product was collected and then alternately washed with distilled water and ethanol to remove organic residues.

3.3. MoS_2@Au Synthesis. Subsequently, MoS_2@AuNPs were obtained using a chemical synthesis process. To incorporate AuNPs, the stock solution was initially obtained by dissolving 0.1 mM $HAuCl_4$ in 10 mL of distilled water under ultrasonication for 10 min. Aqueous sodium citrate tribasic dihydrate (1 wt %, 1 mL) solution was obtained and then mixed with the as-prepared 10 mL solution was magnetically stirred for another 30 min. Further, MoS_2 nanomaterials were added to the abovementioned mixed solution and stirred continuously for 10 min and then washed with ethanol and distilled water twice. The resultant MoS_2@AuNPs were obtained and used for the TERS experiment.

3.4. Modification of MoS_2@AuNPs with Chemical Agent. To prepare samples on silicon (Si) wafer, first, a Si wafer was cut into small squares of about 5 mm × 5 mm each, rinsed with acetone and ethanol, and then dried with nitrogen gas. As-prepared MoS_2 and MoS_2@AuNPs solutions were then dropped onto the precleaned Si wafer and kept at room temperature for 30 min, allowing for the adsorption of nanoparticles onto the surface. Next, 2 mM 4-BTP solution was dropcasted on MoS_2@AuNPs Si wafer and left for 1 h to

https://doi.org/10.1021/acs.jpcc.4c05236
J. Phys. Chem. C XXXX, XXX, XXX−XXX

form a monolayer of 4-BTP molecule on it. The modified sample was then rinsed with ethanol trice to remove the uncoordinated molecules.

3.5. AFM Probe Preparation. First, 240AC series AC mode AFM tips were purchased from Opus MikroMasch USA. The AFM tip parameters are force constant 2 N/m, resonance frequency 70 kHz, and amplitude 20 nm, respectively. Further, AFM tips were modified by metal deposition. For metal deposition, AFM tips were placed in a thermal evaporator (MBrown, Stratham, NH). Metal deposition was conducted at $\sim 1 \times 10^{-6}$ mbar by thermal evaporation of gold (Kurt J. Lesker, Efferson Hills, PA) at 0.1 A/s rate to a final 70 nm Au thickness on the AFM tips. The temperature at the tip surface was ~54 °C upon metal deposition.

3.6. AFM-TER Imaging. An AIST-NT system is equipped to perform the TERS measurement in a side-illumination geometry using a 100× Mitutoyo microscope objective by 633 nm continuous wavelength (CW) laser and a modified AFM tip with a radius of <7 nm*. Scattered electromagnetic radiation was collected using the same objective and directed into the HORIBA iHR550 spectrograph equipped with a Synapse EM-CCD camera (HORIBA, Edison, NJ). During TERS measurements, the system is running in intermittent contact (AC) mode, and the spectra are taken at the moment the tip touches the surface, and the contact time is defined by the spectral acquisition time, which is 2.0 s.

3.7. Materials Characterizations. Field emission-scanning electron microscopy (FE-SEM) imaging was performed using a JEOL scanning electron microscope (JSM- 7500F). X-ray photoelectron spectroscopy (XPS) measurements were performed with a Thermo Scientific instrument with an Al K-α X-ray source.

4. CONCLUSIONS

Using TER, a modern analytical technique that demonstrates single-molecule sensitivity and subnanometer spatial resolution, we examined the optical and catalytic properties of MoS_2 and MoS_2@AuNPs nanomaterials. Using TER, we demonstrated that MoS_2 could be used to dehalogenate and dimerize 4-BTP to form TP and 4,4′-BPDT, respectively. The same reaction products were also observed on MoS_2@AuNPs. However, these plasmonic hybrids provided a much greater yield of 4,4′-BPDT compared with the yield of this molecular analyte on MoS_2. These findings indicate that metal dichalcogenides can catalyze chemical reactions that were previously evident only for noble metal nanomaterials and their bimetallic analogues. We also found that the yield of exciton-driven reactions on such metal dichalcogenides can be enhanced by their decoration with noble metal nanomaterials. These findings open new routes for the synthetic approaches that can be used to fabricate novel catalysts with the desired reactivity and specificity.

■ ASSOCIATED CONTENT

Supporting Information

The Supporting Information is available free of charge at https://pubs.acs.org/doi/10.1021/acs.jpcc.4c05236.

Figure S1. AFM image of the MoS_2 with corresponding *x*- and *y*-axis height profiles; Figure S2. (a) Representative TERS spectra of MoS_2 collected at points in AFM (g), (b) the spectra deconvoluted using Lorenz curve. TERS mapping of MoS_2: (c) E^1 2g, (d) A_{1g}, (e) 2LA(M), and (f) their overlay; Figure S3. AFM image of the 4-BTP modified MoS_2 with corresponding *x*- and *y*-axis height profiles; Figure S4(a) Representative TERS spectra of 4-BTP on the surface of MoS2 nanosheets collected at points in AFM (d), (b, and c) the spectra deconvoluted using Lorenz curves; Figure S5 (a) AFM topography of MoS2 with 4-BTP and AFM-IR absorption maps taken at (b) 1407, (c) 1466, (d) 1543, (e) 1691, and (f) 1734 cm^{-1} on Si-substrate. (g) AFM-IR point spectra taken in the points marked in panel (b) (PDF)

■ AUTHOR INFORMATION

Corresponding Author

Dmitry Kurouski − *Department of Biochemistry and Biophysics, Texas A&M University, College Station, Texas 77843, United States; Department of Biomedical Engineering, Texas A&M University, College Station, Texas 77843, United States;* orcid.org/0000-0002-6040-4213; Email: dkurouski@tamu.edu

Author

Swati J. Patil − *Department of Biochemistry and Biophysics, Texas A&M University, College Station, Texas 77843, United States;* orcid.org/0000-0002-3619-2783

Complete contact information is available at: https://pubs.acs.org/10.1021/acs.jpcc.4c05236

Notes

The authors declare no competing financial interest.

■ REFERENCES

(1) Kumar, N.; Su, W.; Veselý, M.; Weckhuysen, B. M.; Pollard, A. J.; Wain, A. J. Nanoscale Chemical Imaging of Solid-Liquid Interfaces Using Tip-Enhanced Raman Spectroscopy. *Nanoscale* **2018**, *10* (4), 1815−1824.

(2) Klingsporn, J. M.; Jiang, N.; Pozzi, E. A.; Sonntag, M. D.; Chulhai, D.; Seideman, T.; Jensen, L.; Hersam, M. C.; Van Duyne, R. P. Intramolecular Insight into Adsorbate-Substrate Interactions via Low-Temperature, Ultrahigh-Vacuum Tip-Enhanced Raman Spectroscopy. *J. Am. Chem. Soc.* **2014**, *136* (10), 3881−3887.

(3) Cao, Y.; Feng, Y.; Li, C.; Li, W.; Cheng, Y.; Ru, J.; Meng, L.; Sun, M. Plasmonic Gradient and Plexcitonic Effects in Single-Molecule Tip-Enhanced (Resonance) Raman Spectroscopy. *J. Phys. Chem. C* **2023**, *127* (1), 476−489.

(4) Rigor, J.; Kurouski, D.; Large, N. Plasmonic Heating Effects in Tip-Enhanced Raman Spectroscopy (TERS). *J. Phys. Chem. C* **2022**, *126* (32), 13986−13993.

(5) Brongersma, M. L.; Halas, N. J.; Nordlander, P. Plasmon-Induced Hot Carrier Science and Technology. *Nat. Nanotechnol.* **2015**, *10* (1), 25−34.

(6) Li, Z.; El-Khoury, P. Z.; Kurouski, D. Tip-Enhanced Raman Imaging of Photocatalytic Reactions on Thermally-Reshaped Gold and Gold-Palladium Microplates. *Chem. Commun.* **2021**, *57* (7), 891−894.

(7) Li, Z.; Kurouski, D. Nanoscale Structural Characterization of Plasmon-Driven Reactions. *Nanophotonics* **2021**, *10* (6), 1657−1673.

(8) Li, Z.; Kurouski, D. Plasmon-Driven Chemistry on Mono- And Bimetallic Nanostructures. *Acc. Chem. Res.* **2021**, *54* (10), 2477−2487.

(9) Kurouski, D.; Dazzi, A.; Zenobi, R.; Centrone, A. Infrared and Raman Chemical Imaging and Spectroscopy at the Nanoscale. *Chem. Soc. Rev.* **2020**, *49* (11), 3315−3347.

(10) Li, Z.; Kurouski, D. Tip-Enhanced Raman Analysis of Plasmonic and Photocatalytic Properties of Copper Nanomaterials. *J. Phys. Chem. Lett.* **2021**, *12* (34), 8335−8340.
(11) Li, Z.; Kurouski, D. Probing the Redox Selectivity on Au@Pd and Au@Pt Bimetallic Nanoplates by Tip-Enhanced Raman Spectroscopy. *ACS Photonics* **2021**, *8* (7), 2112−2119.
(12) Patil, S. J.; Chodankar, N. R.; Hwang, S. K.; Shinde, P. A.; Seeta Rama Raju, G.; Shanmugam Ranjith, K.; Huh, Y. S.; Han, Y. K. Co-Metal−Organic Framework Derived CoSe2@MoSe2 Core−Shell Structure on Carbon Cloth as an Efficient Bifunctional Catalyst for Overall Water Splitting. *Chem. Eng. J.* **2022**, *429* (September 2021), No. 132379.
(13) Zhang, Z.; Sheng, S.; Wang, R.; Sun, M. Tip-Enhanced Raman Spectroscopy. *Anal. Chem.* **2016**, *88* (19), 9328−9346.
(14) Cao, Y.; Sun, M. Tip-Enhanced Raman Spectroscopy. *Rev. Phys.* **2022**, *8*, No. 100067.
(15) Cheng, H.; Qian, X.; Kuwahara, Y.; Mori, K.; Yamashita, H. A Plasmonic Molybdenum Oxide Hybrid with Reversible Tunability for Visible-Light-Enhanced Catalytic Reactions. *Adv. Mater.* **2015**, *27* (31), 4616−4621.
(16) Guan, H.; Yi, W.; Li, T.; Li, Y.; Li, J.; Bai, H.; Xi, G. Low Temperature Synthesis of Plasmonic Molybdenum Nitride Nanosheets for Surface Enhanced Raman Scattering. *Nat. Commun.* **2020**, *11* (1), No. 3889.
(17) Yin, H.; Kuwahara, Y.; Mori, K.; Cheng, H.; Wen, M.; Huo, Y.; Yamashita, H. Localized Surface Plasmon Resonances in Plasmonic Molybdenum Tungsten Oxide Hybrid for Visible-Light-Enhanced Catalytic Reaction. *J. Phys. Chem. C* **2017**, *121* (42), 23531−23540.
(18) Li, Y.; Hu, Y.; Shi, F.; Li, H.; Xie, W.; Chen, J. C−H Arylation on Nickel Nanoparticles Monitored by In Situ Surface-Enhanced Raman Spectroscopy. *Angew. Chem. - Int. Ed.* **2019**, *58* (27), 9049−9053.
(19) Patil, S. J.; Chodankar, N. R.; Hwang, S. K.; Shinde, P. A.; Rama Raju, G. S.; Ranjith, K. S.; Karekar, S. V.; Huh, Y. S.; Han, Y. K. Two-Dimensional Nanosheets of Bimetallic Chalcogenide-Tagged Nitrogen-Doped Carbon as a Cathode for High-Performance and Durable Zinc-Ion Capacitors. *J. Mater. Chem. A* **2023**, *11* (10), 5112−5126.
(20) Gong, C.; Hu, K.; Wang, X.; Wangyang, P.; Yan, C.; Chu, J.; Liao, M.; Dai, L.; Zhai, T.; Wang, C.; Li, L.; Xiong, J. 2D Nanomaterial Arrays for Electronics and Optoelectronics. *Adv. Funct. Mater.* **2018**, *28* (16), No. 1706559.
(21) Li, Y.; Li, Z.; Chi, C.; Shan, H.; Zheng, L.; Fang, Z. Plasmonics of 2D Nanomaterials: Properties and Applications. *Adv. Sci.* **2017**, *4* (8), 1−25.
(22) Aftab, S.; Hegazy, H. H. Emerging Trends in 2D TMDs Photodetectors and Piezo-Phototronic Devices. *Small* **2023**, *19*, 1−24.
(23) Li, J.; Liu, C. Y.; Liu, Y. Au/Graphene Hydrogel: Synthesis, Characterization and Its Use for Catalytic Reduction of 4-Nitrophenol. *J. Mater. Chem.* **2012**, *22* (17), 8426−8430.
(24) Liu, X.; Liu, L.; Wu, Y.; Wang, Y.; Yang, J.; Wang, Z. Rosette-like MoS2 Nanoflowers as Highly Active and Stable Electrodes for Hydrogen Evolution Reactions and Supercapacitors. *RSC Adv.* **2019**, *9* (24), 13820−13828.
(25) Abid, K.; Belkhir, N. H.; Jaber, S. B.; Zribi, R.; Donato, M. G.; Di Marco, G.; Gucciardi, P. G.; Neri, G.; Maâlej, R. Photoinduced Enhanced Raman Spectroscopy with Hybrid Au@WS2Nanosheets. *J. Phys. Chem. C* **2020**, *124* (37), 20350−20358.
(26) An, J.; Zhao, X.; Zhang, Y.; Liu, M.; Yuan, J.; Sun, X.; Zhang, Z.; Wang, B.; Li, S.; Li, D. Perspectives of 2D Materials for Optoelectronic Integration. *Adv. Funct. Mater.* **2022**, *32* (14), 2110119.
(27) Xia, F.; Wang, H.; Xiao, D.; Dubey, M.; Ramasubramaniam, A. Two-Dimensional Material Nanophotonics. *Nat. Photonics* **2014**, *8* (12), 899−907.
(28) Yao, B.; Huang, S. W.; Liu, Y.; Vinod, A. K.; Choi, C.; Hoff, M.; Li, Y.; Yu, M.; Feng, Z.; Kwong, D. L.; et al. Gate-Tunable Frequency Combs in Graphene-Nitride Microresonators. *Nature* **2018**, *558* (7710), 410−414.
(29) Xue, Y.; Zhang, Y.; Liu, Y.; Liu, H.; Song, J.; Sophia, J.; Liu, J.; Xu, Z.; Xu, Q.; Wang, Z.; et al. Scalable Production of a Few-Layer MoS2/WS2 Vertical Heterojunction Array and Its Application for Photodetectors. *ACS Nano* **2016**, *10* (1), 573−580.
(30) Radisavljevic, B.; Radenovic, A.; Brivio, J.; Giacometti, V.; Kis, A. Single-Layer MoS2 Transistors. *Nat. Nanotechnol.* **2011**, *6* (3), 147−150.
(31) Fang, H.; Chuang, S.; Chang, T. C.; Takei, K.; Takahashi, T.; Javey, A. High-Performance Single Layered WSe 2 p-FETs with Chemically Doped Contacts. *Nano Lett.* **2012**, *12* (7), 3788−3792.
(32) Pei, Z.; Li, J.; Ji, C.; Tan, J.; Shao, Z.; Zhao, X.; Li, Z.; Man, B.; Yu, J.; Zhang, C. Flexible Cascaded Wire-in-Cavity-in-Bowl Structure for High-Performance and Polydirectional Sensing of Contaminants in Microdroplets. *J. Phys. Chem. Lett.* **2023**, *14* (25), 5932−5939.
(33) Shao, M.; Ji, C.; Tan, J.; Du, B.; Zhao, X.; Yu, J.; Man, B.; Xu, K.; Zhang, C.; Li, Z. Ferroelectrically Modulate the Fermi Level of Graphene Oxide to Enhance SERS Response. *Opto-Electronic Adv.* **2023**, *6* (11), 230094−230094.
(34) Bai, S.; Ren, X.; Obata, K.; Ito, Y.; Sugioka, K. Label-Free Trace Detection of Bio-Molecules by Liquid-Interface Assisted Surface-Enhanced Raman Scattering Using a Microfluidic Chip. *Opto-Electronic Adv.* **2022**, *5* (10), 1−10.
(35) Barrabés, N.; Ostolaza, J.; Reindl, S.; Mähr, M.; Schrenk, F.; Drexler, H.; Rameshan, C.; Olszewski, W.; Rupprechter, G. Doped Metal Clusters as Bimetallic AuCo Nanocatalysts: Insights into Structural Dynamics and Correlation with Catalytic Activity by in Situ Spectroscopy. *Faraday Discuss.* **2023**, *242*, 94−105.
(36) Zaera, F. New Advances in the Use of Infrared Absorption Spectroscopy for the Characterization of Heterogeneous Catalytic Reactions. *Chem. Soc. Rev.* **2014**, *43* (22), 7624−7663.
(37) Hess, C. New Advances in Using Raman Spectroscopy for the Characterization of Catalysts and Catalytic Reactions. *Chem. Soc. Rev.* **2021**, *50* (5), 3519−3564.
(38) Rahaman, M.; Rodriguez, R. D.; Plechinger, G.; Moras, S.; Schüller, C.; Korn, T.; Zahn, D. R. T. Highly Localized Strain in a MoS2/Au Heterostructure Revealed by Tip-Enhanced Raman Spectroscopy. *Nano Lett.* **2017**, *17* (10), 6027−6033.
(39) Kato, R.; Umakoshi, T.; Sam, R. T.; Verma, P. Probing Nanoscale Defects and Wrinkles in MoS 2 by Tip-Enhanced Raman Spectroscopic Imaging. *Appl. Phys. Lett.* **2019**, *114* (7), No. 073105.
(40) Rao, V. J.; Matthiesen, M.; Goetz, K. P.; Huck, C.; Yim, C.; Siris, R.; Han, J.; Hahn, S.; Bunz, U. H. F.; Dreuw, A.; et al. AFM-IR and IR-SNOM for the Characterization of Small Molecule Organic Semiconductors. *J. Phys. Chem. C* **2020**, *124* (9), 5331−5344.
(41) Ruggeri, F. S.; Longo, G.; Faggiano, S.; Lipiec, E.; Pastore, A.; Dietler, G. Infrared Nanospectroscopy Characterization of Oligomeric and Fibrillar Aggregates during Amyloid Formation. *Nat. Commun.* **2015**, *6*, No. 1.
(42) Ramer, G.; Ruggeri, F. S.; Levin, A.; Knowles, T. P. J.; Centrone, A. Determination of Polypeptide Conformation with Nanoscale Resolution in Water. *ACS Nano* **2018**, *12* (7), 6612−6619.
(43) Dazzi, A.; Glotin, F.; Carminati, R. Theory of Infrared Nanospectroscopy by Photothermal Induced Resonance. *J. Appl. Phys.* **2010**, *107* (12), No. 124519.
(44) Ruggeri, F. S.; Mannini, B.; Schmid, R.; Vendruscolo, M.; Knowles, T. P. J. Single Molecule Secondary Structure Determination of Proteins through Infrared Absorption Nanospectroscopy. *Nat. Commun.* **2020**, *11* (1), No. 2945.
(45) Zhaliazka, K.; Kurouski, D. Nanoscale Characterization of Parallel and Antiparallel β-Sheet Amyloid Beta 1−42 Aggregates. *ACS Chem. Neurosci.* **2022**, *13* (19), 2813−2820.
(46) Katzenmeyer, A. M.; Aksyuk, V.; Centrone, A. Nanoscale Infrared Spectroscopy: Improving the Spectral Range of the Photothermal Induced Resonance Technique. *Anal. Chem.* **2013**, *85* (4), 1972−1979.
(47) Centrone, A. Infrared Imaging and Spectroscopy beyond the Diffraction Limit*. *Annu. Rev. Anal. Chem.* **2015**, *8*, 101−126.

https://doi.org/10.1021/acs.jpcc.4c05236
J. Phys. Chem. C XXXX, XXX, XXX−XXX

(48) Dou, T.; Li, Z.; Zhang, J.; Evilevitch, A.; Kurouski, D. Nanoscale Structural Characterization of Individual Viral Particles Using Atomic Force Microscopy Infrared Spectroscopy (AFM-IR) and Tip-Enhanced Raman Spectroscopy (TERS). *Anal. Chem.* **2020**, *92* (16), 11297−11304.
(49) Ali, A.; Mangrio, F. A.; Chen, X.; Dai, Y.; Chen, K.; Xu, X.; Xia, R.; Zhu, L. Ultrathin MoS2 Nanosheets for High-Performance Photoelectrochemical Applications: Via Plasmonic Coupling with Au Nanocrystals. *Nanoscale* **2019**, *11* (16), 7813−7824.
(50) Shi, Y.; Huang, J. K.; Jin, L.; Hsu, Y. Te.; Yu, S. F.; Li, L. J.; Yang, H. Y. Selective Decoration of Au Nanoparticles on Monolayer MoS 2 Single Crystals. *Sci. Rep.* **2013**, *3*, No. 1839.
(51) Minh Vuong, N.; Kim, D.; Kim, H. Porous Au-Embedded WO 3 Nanowire Structure for Efficient Detection of CH4 and H2S. *Sci. Rep.* **2015**, *5* (June), No. 11040.
(52) Shi, S.; Sun, Z.; Hu, Y. H. Synthesis, Stabilization and Applications of 2-Dimensional 1T Metallic MoS2. *J. Mater. Chem. A* **2018**, *6* (47), 23932−23977.
(53) Gadelha, A. C.; Santos, J. C. C.; Rabelo, C.; Vasconcelos, T. L.; Alencar, R. S.; Monken, V.; Miranda, H. L. S.; Cury, L. A.; Jaques, Y. M.; Tromer, R. M.; Galvão, D. S.; Cançado, L. G.; Neves, B. R. A.; Jorio, A. Locally-Enhanced Optical Properties in a Hybrid Organic/Inorganic (Coronene/MoS2) Van Der Waals Heterostructure. *2D Mater.* **2023**, *10* (2), 025015.
(54) Wang, C. F.; O'Callahan, B. T.; Arey, B. W.; Kurouski, D.; El-Khoury, P. Z. High-Resolution Raman Nano-Imaging with an Imperfect Probe. *J. Phys. Chem. C* **2022**, *126* (8), 4089−4094.
(55) Madzharova, F.; Heiner, Z.; Kneipp, J. Surface-Enhanced Hyper Raman Spectra of Aromatic Thiols on Gold and Silver Nanoparticles. *J. Phys. Chem. C* **2020**, *124* (11), 6233−6241.
(56) Wang, X.; Huang, S. C.; Huang, T. X.; Su, H. S.; Zhong, J. H.; Zeng, Z. C.; Li, M. H.; Ren, B. Tip-Enhanced Raman Spectroscopy for Surfaces and Interfaces. *Chem. Soc. Rev.* **2017**, *46* (13), 4020−4041.
(57) Wang, R.; He, Z.; Sokolov, A. V.; Kurouski, D. Gap-Mode Tip-Enhanced Raman Scattering on Au Nanoplates of Varied Thickness. *J. Phys. Chem. Lett.* **2020**, *11* (10), 3815−3820.
(58) Plechinger, G.; Heydrich, S.; Eroms, J.; Weiss, D.; Schüller, C.; Korn, T. Raman Spectroscopy of the Interlayer Shear Mode in Few-Layer MoS 2 Flakes. *Appl. Phys. Lett.* **2012**, *101* (10), No. 101906.
(59) Bailo, E.; Deckert, V. Tip-Enhanced Raman Scattering. *Chem. Soc. Rev.* **2008**, *37* (5), 921−930.
(60) Zhan, Z.; Liu, L.; Wang, W.; Cao, Z.; Martinelli, A.; Wang, E.; Cao, Y.; Chen, J.; Yurgens, A.; Sun, J. Ultrahigh Surface-Enhanced Raman Scattering of Graphene from Au/Graphene/Au Sandwiched Structures with Subnanometer Gap. *Adv. Opt. Mater.* **2016**, *4* (12), 2021−2027.
(61) Feng, W.; Chen, L.; Qin, M.; Zhou, X.; Zhang, Q.; Miao, Y.; Qiu, K.; Zhang, Y.; He, C. Flower-like PEGylated MoS2 Nanoflakes for near-Infrared Photothermal Cancer Therapy. *Sci. Rep.* **2015**, *5*, No. 17422.
(62) Liu, R. qing.; Sun, W.; Hu, Y. hua.; Wang, D. zuo. New Collectors for the Flotation of Unactivated Marmatite. *Miner. Eng.* **2010**, *23* (2), 99−103.
(63) Lee, T. W.; Chen, C. C.; Chen, C. Chemical Stability and Transformation of Molybdenum Disulfide Nanosheets in Environmental Media. *Environ. Sci. Technol.* **2019**, *53* (11), 6282−6291.
(64) Sienkiewicz-Gromiuk, J.; Głuchowska, H.; Tarasiuk, B.; Mazur, L.; Rzączyńska, Z. Synthesis, Structural, Spectroscopic and Thermal Characteristics of Disubstituted Biphenyl Derivative: Biphenyl-4,4′-Diacetic Acid. *J. Mol. Struct.* **2014**, *1070* (1), 110−116.
(65) Abhijith, T.; Edappadikkunnummal, S.; Suthar, R.; Thomas, S.; Karak, S. Au-WS2Nanohybrids with Enhanced Optical Nonlinearity for Optical Limiting Applications. *ACS Appl. Nano Mater.* **2022**, *6*, 2327−2335.
(66) Hasz, K.; Hu, Z.; Park, K. D.; Raschke, M. B. Tip-Enhanced Dark Exciton Nanoimaging and Local Strain Control in Monolayer WSe. *Nano Lett.* **2023**, *23* (1), 198−204.
(67) Park, K. D.; Khatib, O.; Kravtsov, V.; Clark, G.; Xu, X.; Raschke, M. B. Hybrid Tip-Enhanced Nanospectroscopy and Nanoimaging of Monolayer WSe2 with Local Strain Control. *Nano Lett.* **2016**, *16* (4), 2621−2627.
(68) Park, K. D.; Raschke, M. B. Polarization Control with Plasmonic Antenna Tips: A Universal Approach to Optical Nanocrystallography and Vector-Field Imaging. *Nano Lett.* **2018**, *18* (5), 2912−2917.
(69) Park, K. D.; Jiang, T.; Clark, G.; Xu, X.; Raschke, M. B. Radiative control of dark excitons at room temperature by nano-optical antenna-tip Purcell effect. *Nat. Nanotechnol.* **2018**, *13* (1), 59−64.
(70) Karthick Kannan, P.; Shankar, P.; Blackman, C.; Chung, C. H. Recent Advances in 2D Inorganic Nanomaterials for SERS Sensing. *Adv. Mater.* **2019**, *31* (34), 1−27.
(71) Quan, Y.; Yao, J.; Yang, S.; Chen, L.; Li, J.; Liu, Y.; Lang, J.; Shen, H.; Wang, Y.; Wang, Y.; et al. ZnO Nanoparticles on MoS2Microflowers for Ultrasensitive SERS Detection of Bisphenol A. *Microchim. Acta* **2019**, *186* (8), 4−11.
(72) Lin, S.; Mandavkar, R.; Burse, S.; Habib, M. A.; Khalid, T.; Joni, M. H.; Chung, Y. U.; Kunwar, S.; Lee, J. MoS2 Nanoplatelets on Hybrid Core-Shell (HyCoS) AuPd NPs for Hybrid SERS Platform for Detection of R6G. *Nanomaterials* **2023**, *13* (4), 769.
(73) Patil, S. J.; Kurouski, D. Tip-Enhanced Raman Imaging of Plasmon-Driven Dimerization of 4- Bromothiophenol on Nickel Decorated Gold Nanoplates Bimetallic Nanostructures. *Chem. Commun.* **2023**, *59*, 10976−10979.

https://doi.org/10.1021/acs.jpcc.4c05236
J. Phys. Chem. C XXXX, XXX, XXX−XXX